Efficient ethylene electrosynthesis through C–O cleavage promoted by water dissociation

Yongxiang Liang [1,2,5], Feng Li [3,5], Rui Kai Miao [3,5], Sunpei Hu[2], Weiyan Ni[1], Shuzhen Zhang [4], Yanjiang Liu[1], Yang Bai [1], Haoyue Wan [1], Pengfei Ou[1], Xiao-Yan Li [1], Ning Wang[1], Sungjin Park[1], Fengwang Li [4] ✉, Jie Zeng [2] ✉, David Sinton[3] ✉ & Edward H. Sargent [1] ✉

Electrochemical reduction of carbon monoxide is a promising carbonate-free approach to produce ethylene using renewable electricity. However, the performance of this process suffers from low selectivity and energy efficiency. A priority has been to weaken water dissociation with the aim of inhibiting the competing hydrogen evolution reaction but when this path was examined by replacing H_2O with D_2O, a further-reduced selectivity toward ethylene was observed. Here we examine approaches to promote water adsorption and to decrease the energy barrier to the ensuing water dissociation step, which could promote C–O cleavage in *CHCOH hydrogenation to *CCH. We modified a copper catalyst with the strong electron acceptor 7,7,8,8-tetracyanoquinodimethane, which made the catalyst surface electron deficient. The observed ethylene Faradaic efficiency was 75%, 1.3 times greater than that of unmodified copper control catalysts. A full-cell energy efficiency of 32% was achieved for a total projected energy cost of 154 GJ t^{-1} in ethylene electrosynthesis in a membrane electrode assembly.

The reduction of carbon dioxide (CO_2RR) to chemicals such as ethylene (C_2H_4) using renewable electricity may contribute to industrial decarbonization[1–5]. Alkaline CO_2RR enables efficient carbon–carbon coupling; however, carbonate formation in alkaline condition leads to inefficient CO_2 utilization[6]. Approaches such as performing the CO_2RR in acidic electrolytes and utilizing bipolar membranes to regenerate CO_2 have been used to tackle the issue of CO_2 loss, but the acidic approach has to date suffered from a lower energy efficiency (~10%

towards C_2H_4), in part because carbon–carbon coupling is less favoured under these conditions[7], and the bipolar membrane approaches typically add appreciable excess voltage[8].

Carbon monoxide electroreduction (CORR) offers an energy-efficient and carbonate-free route towards C_2H_4 (refs. 9–11). However, there remains a need to increase further the energy efficiency (EE) of CO-to-C_2H_4 electrosynthesis from its current best value of 28%, achieved at a current density of 170 mA cm^{-2} (ref. 12).

[1]The Edward S. Rogers Department of Electrical and Computer Engineering, University of Toronto, Toronto, Ontario, Canada. [2]Hefei National Research Center for Physical Sciences at the Microscale, CAS Key Laboratory of Strongly-Coupled Quantum Matter Physics, Key Laboratory of Surface and Interface Chemistry and Energy Catalysis of Anhui Higher Education Institutes, Department of Chemical Physics, University of Science and Technology of China, Hefei, P.R. China. [3]Department of Mechanical and Industrial Engineering, University of Toronto, Toronto, Ontario, Canada. [4]School of Chemical and Biomolecular Engineering and ARC Centre of Excellence for Green Electrochemical Transformation of Carbon Dioxide, The University of Sydney, Sydney, New South Wales, Australia. [5]These authors contributed equally: Yongxiang Liang, Feng Li, Rui Kai Miao. ✉e-mail: fengwang.li@sydney.edu.au; zengj@ustc.edu.cn; dave.sinton@utoronto.ca; ted.sargent@utoronto.ca
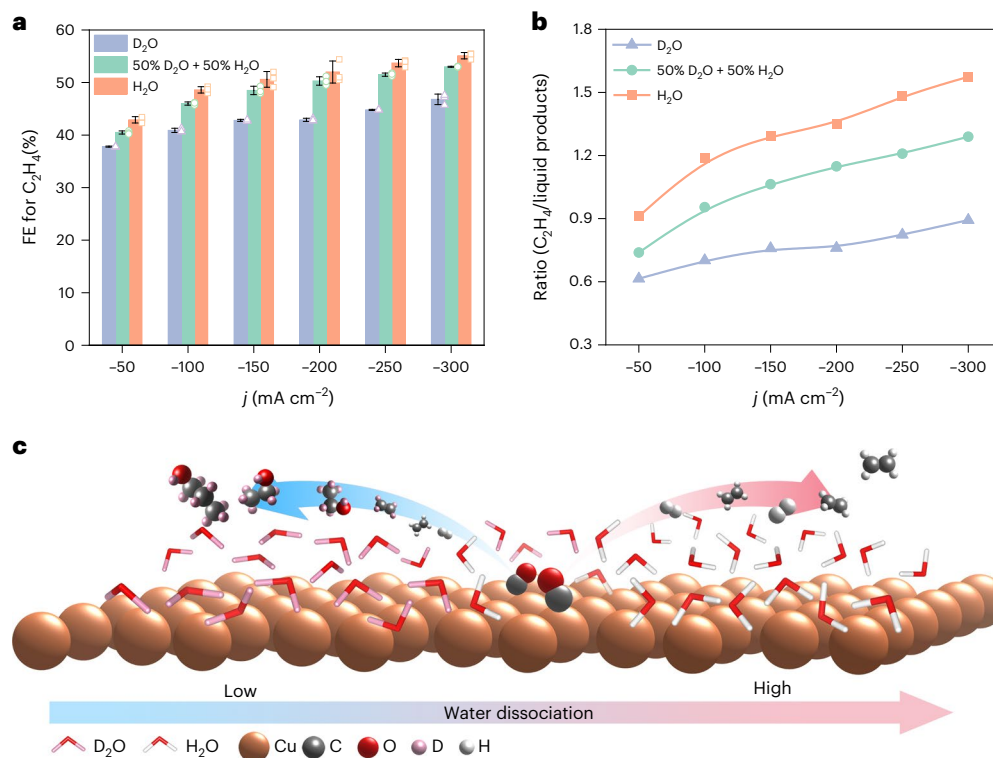
Fig. 1 | Influence of water dissociation on the product distribution in the CORR. a, FE for C_2H_4 (C_2D_4) over commercial 25 nm copper nanoparticles under different applied current densities in D_2O/1 M LiOH, 50% D_2O + 50% H_2O/1 M LiOH and H_2O/1 M LiOH electrolyte. The error bars represent the s.d. of three independent experiments and the corresponding data distribution is presented by hollow points. Data are presented as mean ± s.d. **b**, Ratio of C_2H_4 (C_2D_4) to liquid products in D_2O/1 M LiOH, 50% D_2O + 50% H_2O/1 M LiOH and H_2O/1 M LiOH electrolyte. **c**, Our hypothesis about the effect of water dissociation on product distribution in the CORR: H_2 formation exhibited a similar selectivity trend with respect to C_2H_4, that is, accelerating water dissociation promoted H_2 and C_2H_4.

An avenue to increase production of multicarbon (C_{2+}) products has been to focus on alkaline electrolytes with the goal of slowing the competing hydrogen evolution reaction (HER)[13–15]. HER kinetics decrease by orders of magnitude in alkaline electrolyte compared with acid electrolyte, a change linked to the high activation barrier of the alkaline Volmer step ($H_2O + e^- \rightarrow$ *H + OH$^-$) which is reliant on the cleavage of a H–OH bond in water dissociation[16–18].

In this work, we explored the product distribution in CORR with different rates of water dissociation. In control experiments, we found that there is a decreased C_2H_4 selectivity when the water dissociation was slowed. This finding motivated us to further accelerate water dissociation to improve the single product (C_2H_4) selectivity. By molecular modification of copper catalysts with 7,7,8,8-tetracyanoquinodimethane (TCNQ), a strong electron acceptor, we achieved a C_2H_4 Faradaic efficiency (FE) of 75% at 500 mA cm^{-2} in a flow cell, 1.3 times greater than unmodified copper control catalysts. The performance evaluation in a membrane electrode assembly (MEA) system showed a full-cell EE of 32% to C_2H_4, corresponding to an energy cost of 154 GJ t^{-1} for C_2H_4 electrosynthesis. A series of operando characterization and density functional theory (DFT) calculations revealed that the strong interaction between copper and TCNQ enhances water adsorption and dissociation. This decreases the energy barrier to hydrogenation of a key intermediate, *CHCOH to *CCH, in the CO-to-C_2H_4 pathway, and thereby improves C_2H_4 selectivity in CORR.

Results and discussion

Influence of water dissociation on CORR product distribution

We began with a study of the competition for hydrogen from water dissociation, looking at CORR-to-C_2H_4 versus HER. Using a copper catalyst operating in a flow cell (Supplementary Figs. 1 and 2), we tuned water dissociation by altering the ratio of H_2O to D_2O in 1 M LiOH electrolyte.

The FE for H_2 (D_2) decreased when the D_2O proportion increased; the D_2 FE was <1% in pure D_2O (Supplementary Fig. 3), a finding we attribute to the sluggish dissociation of D_2O (refs. 19,20). The C_{2+} FE increased with the decrease in H_2 (D_2) FE.

However, it was noted that the C_2H_4 FE decreased as the D_2O content was increased (Fig. 1a). In addition, the ratio of C_2H_4 to oxygenated liquid products increased with H_2O content in the mixed electrolyte. This ratio increased with voltage and current and reached 1.6 in H_2O/1 M LiOH electrolyte at 300 mA cm^{-2} (Fig. 1b). The Tafel slope (~120 mV per decade) and the kinetic isotope effect (KIE) (1.6–1.9) for C_2H_4 in all three electrolytes implicate the involvement of water in the rate-determining step (RDS) of the CO-to-C_2H_4 pathway (Supplementary Fig. 4)[21–23]. H_2 formation exhibited a similar selectivity trend with respect to C_2H_4, that is, accelerating water dissociation promoted H_2 and C_2H_4 (Fig. 1c).

Catalyst characterization and CORR performance

These initial studies motivated us to examine how to increase water dissociation in the CORR. Previous reports showed that water dissociation kinetics in an alkaline HER could be increased by constructing electron-deficient active metal sites with unfilled *d* orbitals to immobilize the oxygen atom in water via stronger electrostatic affinity[24–27]. We sought molecular means to increase water dissociation at the heterogeneous catalyst surface and reasoned that a strong electron acceptor could contribute to this goal.

We therefore investigated TCNQ, a strong electron acceptor[28,29]. Neutral, planar TCNQ accepts two electrons from copper to aromatize the central hexagonal ring and reduce both dicyanomethylene groups to the anionic form, TCNQ^{2-} (Fig. 2a)[30].

With improved performance in the CORR as our ultimate target, a baseline/reference catalyst comprised of copper oxide (CuO) nanosheets synthesized via a hydrothermal method was developed
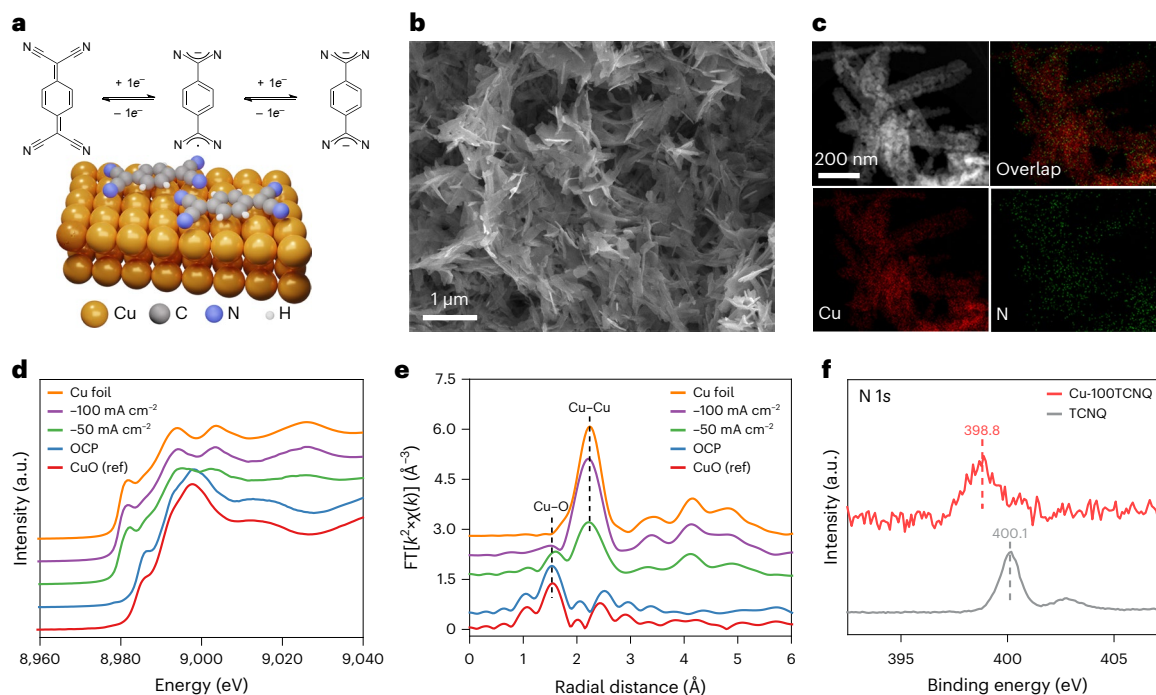
Fig. 2 | Characterization of Cu-100TCNQ catalyst. a, Schematic illustration of copper with TCNQ modification during the CORR. Yellow, grey, blue and white balls represent copper, carbon, nitrogen and oxygen atoms, respectively. **b**, Scanning electron microscopy image of Cu-100TCNQ. **c**, Scanning transmission electron microscopy image and corresponding energy-dispersive X-ray spectroscopy mapping images (copper and nitrogen) of Cu-100TCNQ. **d,e**, Operando X-ray absorption spectroscopy analysis for the CuO–TCNQ complex electrode obtained during the electrochemical polarization at different applied current densities: normalized X-ray absorption near-edge structure spectra at the Cu K-edge (**d**), and the Fourier transform (FT) of the extended X-ray absorption fine structure spectra (**e**). The spectra of reference of CuO and copper foil are included for comparison. The open circuit potential is defined as OCP. **f**, High-resolution N 1s XPS spectra of Cu-100TCNQ and TCNQ molecule.

(see Methods for details; Supplementary Figs. 5 and 6), and the as-synthesized CuO exhibited a CORR-to-C_2H_4 FE typically ~5% (absolute) greater than that of commercial copper nanoparticles (Supplementary Fig. 7). TCNQ was then incorporated into the catalyst by in situ electroreduction of a mixture of CuO and TCNQ, giving Cu-100TCNQ. Cu-100TCNQ exhibited no significant changes in morphology (Fig. 2b and Supplementary Fig. 8) or crystalline reconstruction (Supplementary Fig. 9) compared to CuO-derived bare copper electrodes. Scanning transmission electron microscopy energy-dispersive X-ray spectroscopy mapping shows that copper and nitrogen elements were distributed uniformly in Cu-100TCNQ (Fig. 2c and Supplementary Fig. 10). Operando X-ray absorption near-edge structure results of Cu-100TCNQ revealed the phase transformation of CuO to metallic copper at applied current densities of −50 mA cm^{-2} to −100 mA cm^{-2} in the CORR (Fig. 2d). This conversion was also observed in Fourier-transform extend X-ray absorption fine structure results, in which the peak ascribed to Cu–O was converted to Cu–Cu coordination (Fig. 2e). High-resolution X-ray photoelectron spectroscopy (XPS) spectra of nitrogen and copper in Cu-100TCNQ suggest the transfer of electrons from copper to TCNQ (Fig. 2f and Supplementary Fig. 11), consistent with the electron paramagnetic resonance spectra (Supplementary Fig. 12)[31]. These results suggested that the copper of Cu-100TCNQ existed in a crystalline metallic phase and the anionic TCNQ^{2-} bonded the copper atoms by nitrogen in the cyano group, resulting in an electron-deficient copper surface during the CORR.

In the CORR, the product distribution (C_2H_4, ethanol, n-propanol, acetate (AcO$^-$) and H_2) shows C_{2+} FE >90%, with C_2H_4 the dominant product (Fig. 3a). The FE for C_2H_4 increased with applied current density, while the FE towards ethanol and n-propanol decreased. TCNQ modification led to a peak ethylene FE of 75% at 500 mA cm^{-2}, compared with 60% for copper. The ratio of C_2H_4 to oxygenated liquid products for Cu-100TCNQ was 2.3× higher than for copper (Fig. 3b).

A zero-gap MEA electrolyser was then used to minimize the full cell voltage (Supplementary Fig. 13). Nickel–iron–boron (NiFe-B) catalyst was used to substitute commercial IrO$_2$ for anodic oxygen evolution (Supplementary Fig. 14)[32], and a full cell voltage of 2.39 V was obtained at 500 mA cm^{-2} (Supplementary Fig. 15). The gas product distribution was similar when different anode catalysts were used (Supplementary Table 1), except that ethanol and n-propanol were further oxidized to AcO$^-$ and propionic acid, respectively, on the NiFe-B (Supplementary Figs. 16–18 and Supplementary Table 2)[33]. The EE for C_2H_4 reached a peak value of 32% with a C_2H_4 partial current density of 442 mA cm^{-2} (Fig. 3c and Supplementary Table 3). The optimized single-pass carbon efficiency (SPCE) for C_2H_4 was 80% when the flow rate decreased to 1.6 sccm (Fig. 3d). In comparison with reported CO$_2$RR/CORR catalysts, Cu-100TCNQ exhibited superior performance in terms of FE and EE for C_2H_4 (Fig. 3e and Supplementary Table 4). In stability studies, the catalyst retained FE$_{C2H4}$ greater than 70% for >100 h at 500 mA cm^{-2} (Fig. 3f), with TCNQ remaining on the copper catalyst for the duration (Supplementary Fig. 19). A technoeconomic analysis was performed to assess the economic feasibility of C_2H_4 electrosynthesis using the cascade CO$_2$RR model (Supplementary Fig. 20 and Supplementary Note 1). The result is an estimated energy cost of 154 GJ t^{-1} in the electrified production of C_2H_4 (Fig. 3g, Supplementary Fig. 21, Supplementary Note 2 and Supplementary Table 5).

Reaction mechanism studies

Operando Raman measurements were used to investigate adsorbed CO (*CO) in each catalyst because *CO is a common intermediate for C_{2+} products[34]. Linear sweep voltammetry (LSV) curves indicated that the modification of TCNQ accelerated the carbon–carbon coupling over Cu-100TCNQ in the CORR (Supplementary Fig. 22). Raman features at 1,900–2,200 cm^{-1} correspond to C–O stretching (Supplementary Fig. 23)[35], and include two *CO configurations, the low-frequency linear
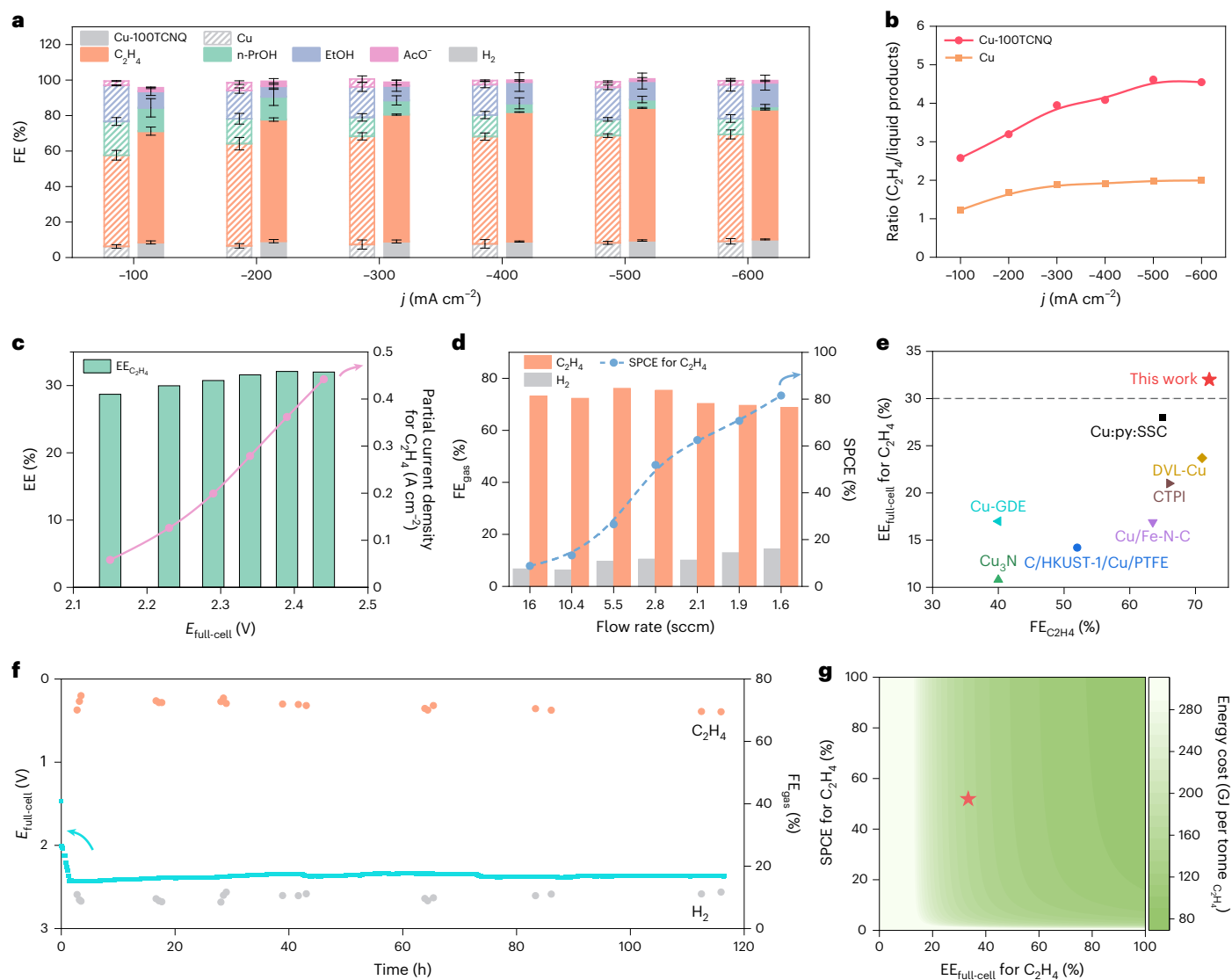
Fig. 3 | CORR performance of TCNQ-modified copper electrocatalyst.
a, FE for all products under different applied current densities over bare copper (patterned) and Cu-100TCNQ (solid filled) in a flow cell. The error bars represent the s.d. of three independent experiments. Data are presented as mean ± s.d. **b**, The ratio of C_2H_4 to oxygenated liquid products over copper and Cu-100TCNQ in a flow cell. **c**, The optimized full-cell EE and partial current densities for C_2H_4 over Cu-100TCNQ catalyst under different applied potentials. **d**, The FE for C_2H_4 and H_2 and the corresponding SPCE for C_2H_4 over Cu-100TCNQ with decreasing flow rate. **e**, Comparison of the maximum FE and EE for C_2H_4 over Cu-100TCNQ and state-of-the-art CO_2/CO catalysts. DVL-Cu, dense vertical lamellate Cu; CTPI, Cu/tetrahydro-phenanthrolinium/ionomer; Cu-GDE, Cu gas diffusion electrode; Cu:py:SSC, Cu:N-tolyl substituted tetrahydro-bipyridine:short-side-chain ionomer. **f**, Stability of Cu-100TCNQ at a constant applied current density of 500 mA cm^{-2} and the corresponding FE for C_2H_4 and H_2. **g**, The influence of EE and SPCE for C_2H_4 on the energy cost for electrosynthesis of C_2H_4. The red star represents the minimum energy cost for electrosynthesis of C_2H_4 at a flow rate of 2.8 sccm in this work.

band CO (LFB-CO) at 2,060 cm^{-1} and the high-frequency linear band CO (HFB-CO) at 2,095 cm^{-1}. The LFB-CO peak exhibited a dynamic shift in response to applied potential, that is, Stark tuning[36], while the inert HFB-CO remained constant. The LFB-CO to HFB-CO ratio was eight times higher for Cu-100TCNQ compared with bare copper, suggesting a weakened C=O bond favourable for carbon–carbon coupling[37], consistent with the LSV result. The dramatic changes of CO adsorption configurations were attributed to the electron-deficient copper surface induced by TCNQ modification[38].

These observations account for the high C_{2+} formation rate; we now turn to discuss the origins of the high C_2H_4 production specifically. The D_2O control experiments highlighted the influence of water dissociation on C_2H_4 selectivity (Supplementary Fig. 24). The Tafel slope (-120 mV per decade) and the kinetic isotope effect (1.5) for C_2H_4 over Cu-100TCNQ indicate that TCNQ modification does not change the rate-determining step over copper in the CO-to-C_2H_4 pathway but accelerates the water-dissociation

process (Supplementary Fig. 25). The performance was studied as a function of the surface concentration of TCNQ. The surface treatment does not noticeably impact the copper morphology (Supplementary Fig. 26) or the local chemical environment near the electrodes (Supplementary Figs. 27 and 28). When the TCNQ concentration was increased further, the peak FE_{C2H4} declined (Supplementary Fig. 29). LSV under argon revealed that, as a function of TCNQ surface concentration, Cu-100TCNQ had the highest HER activity (Fig. 4a), again consistent with the idea that water dissociation is enhanced in Cu-100TCNQ.

DFT calculations suggest that TCNQ adsorbed on copper takes on a bent conformation, with the cyano groups oriented towards the copper atoms beneath via Cu–N chemical bonding, and with the carbon ring positioned parallel to the copper surface (Supplementary Fig. 30). The binding energy of H_2O on Cu(111)-TCNQ (−0.7 eV) is lower than that on Cu(111) (−0.4 eV), that is, H_2O adsorbs more strongly on Cu(111)-TCNQ (Fig. 4b and Supplementary Fig. 31). From DFT, TCNQ lowers the water
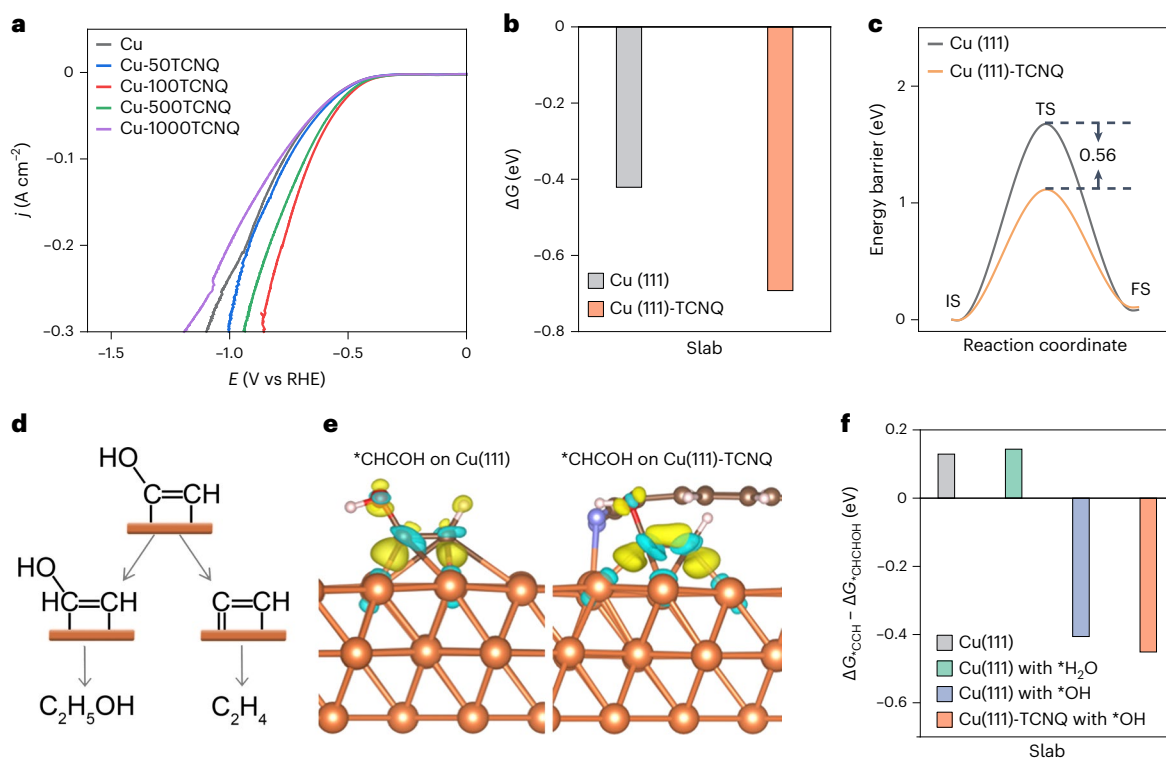
Fig. 4 | Mechanistic study of TCNQ modification of copper for C_2H_4 formation. **a**, LSV curves of copper, Cu-50TCNQ, Cu-100TCNQ, Cu-500TCNQ and Cu-1000TCNQ under argon atmosphere. **b**, H_2O adsorption energy over Cu(111)-TCNQ and Cu(111) surfaces. **c**, H_2O dissociation energy barrier over Cu(111)-TCNQ and Cu(111) surfaces. IS, initial state; TS, transition state; FS, final state. **d**, Schematic representation of the mechanism depicting the influence of carbon–oxygen bond strength in *CHCOH on the selectivity of C_2H_4 and ethanol. **e**, Charge-density difference of *CHCOH on Cu(111)-TCNQ and Cu(111) surfaces. Yellow and blue contours represent the isosurfaces of electronic charge accumulation and depletion, respectively, with an isosurface value of 0.01 e $Å^{-3}$ implemented. **f**, Reaction free-energy difference between *CCH and *CHCHOH on Cu(111), Cu(111) with *H_2O and Cu(111) with *OH surfaces, and Cu(111)-TCNQ with *OH slabs, respectively.

dissociation barrier (ΔE_B) (1.12 eV) compared with Cu(111) (1.68 eV) (Fig. 4c and Supplementary Fig. 32). Raman spectroscopy also showed enhanced water dissociation in the CORR based on adsorbed OH (*OH) on copper (Cu–OH), 490–600 cm^{-1}, during the water dissociation (H–OH cleavage) process (Supplementary Fig. 33), corresponding to the DFT results (Supplementary Fig. 34). In ab initio molecular dynamics simulations, *OH exerts a strong attractive force on the H_2O layer, bringing H_2O closer to the surface and activating H_2O as indicated by a lengthened O–H bond (Supplementary Fig. 35).

Using DFT, we studied the effect of water dissociation on post-hydrogenation of the *CHCOH intermediate—the key post carbon–carbon coupling intermediate that branches C_2H_4 and ethanol pathways—in the CORR (Fig. 4d)[39,40]. The evolution of related intermediates occurs on active copper sites, not on the TCNQ molecule (Supplementary Figs. 36 and 37). From the electronic configuration of *CHCOH on Cu(111)-TCNQ versus bare Cu(111), we see that the charge density of the C–O bond decreases when the *CHCOH is adsorbed on the Cu(111)-TCNQ surface, that is, the C–O bond is weakened after TCNQ modification (Fig. 4e). With water dissociation kinetics accelerated by the TCNQ molecule, the reaction pathway of *CHCOH to *CCH for C_2H_4, involving the breaking of the C–O bond, exhibits a more favourable Gibbs free energy compared with the *CHCOH to *CHCHOH pathway for ethanol (Fig. 4f and Supplementary Fig. 38). We concluded that the TCNQ modification enhanced water dissociation, further promoting the hydrogenation of *CHCOH to *CCH by breaking the C–O bond, thereby improving the C_2H_4 selectivity in the CORR.

Conclusions

This study showcases a design principle based on activating water dissociation to promote the CO-to-C_2H_4 pathway in the CORR. When we use the strong electron acceptor TCNQ to modify copper, we obtain evidence that the interaction between copper and TCNQ enhances water adsorption and water dissociation. This decreases the energy barrier to hydrogenation of a key intermediate, *CHCOH to *CCH, in the CO-to-C_2H_4 pathway, and contributes to improving C_2H_4 selectivity in the CORR. These advances enable us to report a C_2H_4 FE of 75% at 500 mA cm^{-2} in a flow cell. A MEA system showed an EE of 32% to C_2H_4, corresponding to an energy cost of 154 GJ t^{-1} for C_2H_4 electrosynthesis. This work adds an added degree of freedom in the design of catalysts for the selective and energy-efficient production of multicarbon products.

Methods

Chemicals and materials

Copper(II) chloride dihydrate (CuCl$_2$·H_2O, 99.95%), sodium dodecyl benzenesulfonate (CH$_3$(CH$_2$)$_{11}$C$_6$H$_4$SO$_3$Na, AR), TCNQ (98%), anhydrous acetonitrile (CH$_3$CN, 99.8%), lithium hydroxide (LiOH, 99.9%), anhydrous iron(III) chloride (FeCl$_3$, ≥99.99%), nickel(II) chloride hexahydrate (NiCl$_2$·6H_2O, 99.9%), sodium borohydride (NaBH$_4$, ≥98.0%), copper foil (99.98%), Nafion perfluorinated resin solution (5 wt% in a mixture of lower aliphatic alcohols and water, contains 45% water), ethanol (≥99.5%), methanol (≥99.5%), deuterium oxide (D$_2$O, 99.9%) and dimethylsulfoxise (DMSO, anhydrous, ≥99.9%) was purchased from Sigma-Aldrich. Sodium hydroxide (NaOH, GR) was purchased from Caledon Laboratory Chemical. Copper (nanopowder, 25 nm particle size) was purchased from US Research Nanomaterials. Sustainion x37-50-grade-60 anion-exchange membranes were purchased from Dioxide Materials; anion-exchange membranes Fumasep FAB-PK-130, Pention-D18-5 wt% dispersion and Teflon PTFE DISP 30 fluoropolymer dispersion, and carbon paper-based gas diffusion layers (Freudenberg H23C3) were purchased from Fuel Cell Store. Commercial iridium

oxide (IrO_2) anode (titanium fibre felt, 200 mm × 100 mm × 0.3 mm, fibre felt coated with Ir-mixed metal oxide (MMO)) was purchased from Magneto Special Anodes. Ultrapure Millipore water (resistivity, 18.2 MΩ cm) was used for all experiments. All chemicals were used without further purification.

Synthesis of CuO nanosheets

The synthesis of CuO nanosheets was carried out using a modified hydrothermal method[41]. First, 1.70 g of $CuCl_2 \cdot 2H_2O$ and 3.48 g of $CH_3(CH_2)_{11}C_6H_4SO_3Na$ were dissolved into 25 ml of deionized water, while stirring continuously at 25 °C. Then, 15 ml of 4 M NaOH was slowly added to the solution. The resulting dark blue solution was placed in a 50 ml Teflon-lined stainless autoclave and subjected to a hydrothermal reaction for 24 h at 120 °C in an oven. After cooling to room temperature, a black precipitate was obtained, which was then washed three times with water and ethanol, centrifuged and dried. Finally, the powder was sintered at 300 °C for 2 h in air to eliminate any residual organic matter.

Preparation of the Cu-x (x = 0, 50, 100, 500, 1000) TCNQ electrodes

To prepare the TCNQ/CH_3CN solution, TCNQ was dissolved in CH_3CN at a concentration of 10 mM. Next, 20 mg of CuO powder was dispersed in 3 ml of methanol. Then, 100 μl of TCNQ/CH_3CN was added to the above mixture under ultrasonication for 30 min, after which 80 μl of Nafion was added, and the mixture was ultrasonicated for another 1 h to prepare the ink. The resulting suspension was spray-coated onto a 3 cm × 3 cm H23C3 carbon paper to prepare the CuO-100TCNQ electrode with a loading amount of 1 mg cm^{-2}. The Cu-100TCNQ electrode was prepared by in situ electroreducing the CuO-100TCNQ under the CORR conditions. The preparation of the copper, Cu-50TCNQ Cu-500TCNQ and Cu-1000TCNQ electrodes followed a similar process, except that 0 μl, 50 μl, 500 μl and 1000 μl TCNQ/CH_3CN solution were added to the ink, respectively.

Preparation of NiFe-B anode electrodes

The NiFe-B catalysts were synthesized using a reported method with slight modification[32]. Specifically, $NiCl_2 \cdot 6H_2O$ (332.8 mg) and anhydrous $FeCl_3$ (227.1 mg) were dissolved in 2 ml of deionized water. In a separate vial, a solution of $NaBH_4$ (2 ml, 5 M) in water was prepared. To prevent uncontrolled hydrolysis that may lead to the formation of precipitates, all solutions were cooled in an ice bath for 10 min. The nickel and iron precursors were then added dropwise to a 2 ml $NaBH_4$ aqueous solution. The resulting black solution was washed and centrifuged with water and ethanol three times before vacuum drying.

To prepare the ink for the NiFe-B anode electrodes, 80 mg of the NiFe-B powder, 200 μl of Pention-D18-5 wt% dispersion and 640 μl of PTFE aqueous solution (PTFE DISP 30 fluoropolymer dispersion diluted to 10 mg ml^{-1}) were dispersed in 6 m of methanol under ultrasonication for 1 h. The resulting suspension was then spray coated onto 2.5 cm × 5 cm IrO_2 with a loading amount of 3 mg cm^{-2}.

Electrochemical experiments

The CORR experiments were carried out using a three-electrode flow cell electrolyser or MEA, as illustrated in the detailed sketches (Supplementary Figs. 2 and 13). In the flow cell, the cathode consisted of a gas diffusion electrode, and the anode was made of platinum mesh. A reference electrode filled with saturated KCl solution and made of Ag/AgCl was used. To prevent product crossover, an anion-exchange membrane (Fumasep FAB-PK-130) was utilized to separate the catholyte and anolyte compartments. The Autolab PGSTA204 module from Metrohm Autolab, along with a BOOSTER10A module, was used as the power supply for the experiments. Alkaline solution with 1 M LiOH electrolyte was used as the electrolyte at both the cathode and anode side, and the cathode and anode compartments were supplied with the electrolyte separately using two variable-speed peristaltic tubing pumps. A flow of 20 sccm CO gas was directed towards the catholyte interface through the gas

diffusion layer. LSV data were collected by sweeping the electrode in the flow cell at a scan rate of 100 mV s^{-1} under a N_2 and CO atmosphere.

All the applied cathode potentials in the flow cell were converted to the reversible hydrogen electrode (RHE) reference scale with a standard compensation by:

$$E(\text{V vs RHE}) = E(\text{V vs Ag/AgCl}) + 0.197 + 0.059 \times \text{pH} - 90\% \times i \times R$$

where the pH is 14 for 1 M LiOH electrolyte and R is the solution resistance, which was determined to be 5.2 Ω in 1 M LiOH electrolyte from Nyquist plots (Supplementary Fig. 39). A factor of 90% was applied for iR compensation during flow cell operation. The CORR in D_2O, 50% D_2O + 50% H_2O (volume ratio, 1:1) electrolyte was performed with similar procedures except for replacing H_2O with D_2O, where the pH in 50% D_2O + 50% H_2O/1 M LiOH and D_2O/1 M LiOH electrolyte was 14.35 and 14.95, respectively. R was determined to be 5.7 Ω, and 6.4 Ω in 50% D_2O + 50% H_2O/1 M LiOH and D_2O/1 M LiOH electrolyte, respectively.

The MEA was composed of a cathode electrode, an IrO_2 (or NiFe-B) anode electrode and an anion-exchange membrane (Sustainion X37-50-grade 60). The electrochemical testing cell was assembled by placing the membrane between the cathode and anode electrode, in which the catalyst layers of both electrodes were facing the membrane. The anode catalyst was protected and surrounded by a 0.02-inch-thick gasket for electrical insulation. The reaction area was regulated by the pore area in the gasket, which was set at 1 cm^2. This assembly was then inserted into a fuel cell device from Dioxide Material, which had serpentine flow channels that were equally compressed with torque applied to the bolts. A constant rate of 15 ml min^{-1} of 1 M LiOH anolyte flowed through the anodic channel, and a digital mass flow meter supplied the humidified CO feed gas to the cathodic channel at a constant rate of 20 sccm. After the electrolyser assembly, a galvanostatic method was used to apply the electrolysis, and the current density was gradually increased from an initial 50 mA cm^{-2} in increments of 50 mA cm^{-2}. The current increments were made upon complete stabilization of the corresponding voltage. For the stability test, the MEA was operated at a constant full-cell current density of 500 mA cm^{-2}, and 1 litre of 1 M LiOH electrolyte was prepared to ensure that the electrolyte composition remained constant during the long electrolysis process.

The gas products were collected in 1 ml volumes using gas-tight syringes (Hamilton chromatography syringe) and then injected into an offline gas chromatograph (GC2014, Shimadzu) for analysis. The gas chromatograph used for gas product analysis had two detectors: a flame ionization detector was used to detect C_2H_4, and a thermal conductivity detector was used to detect H_2. The spectra obtained from the gas chromatograph for each gas injection were used to calculate the FE towards the gas product of the CORR.

Liquid products were analysed by ^1H NMR spectroscopy (600 MHz, Aligent DD2 spectrometer) with water suppression, in which 0.1 ml of the electrolyte was mixed with 0.1 ml DMSO (internal standard, diluted to 100 ppm (m/m) by D_2O) and 0.4 ml D_2O. For a specific liquid product, denoted as p (n-propanol, ethanol, acetate), the FE of the liquid product was calculated as follows.

The number of moles of liquid product, n_p, in the NMR tube is determined by the following formula:

$$n_p = \frac{s_p \times H_{DMSO}}{s_{DMSO} \times H_p} \times \frac{c_{DMSO} \times m_{DMSO}}{78.1}$$

where S_p and S_{DMSO} are the integrated areas of the product and DMSO peaks in the ^1H NMR spectrum, respectively; H_{DMSO} and H_p are the numbers of hydrogen with the chemical shift for a specific functional group (H_{DMSO} = 6 for two $-CH_3$ in DMSO, $H_{n\text{-propanol}}$, $H_{ethanol}$, $H_{acetate}$ = 3 for one $-CH_3$ in one molecule); c_{DMSO} is the concentration of DMSO in the internal standard; and m_{DMSO} is the mass of the internal standard. The molar mass of DMSO is 78.1 g mol^{-1}.

The FE of the liquid product, FE_p, is calculated as follows:

$$FE_p = \frac{\frac{n_p \times m_{electrolyte}}{m_t} \times e_p \times F}{C_{total}} \times 100\%$$

where $m_{electrolyte}$ is the total mass of electrolyte in the cathode side of flow cell; m_t is the mass of electrolyte in the NMR tube; e_p is the number of electrons transferred per molecule ($e_{n\text{-propanol}} = 12$; $e_{ethanol} = 8$; $e_{acetate} = 4$); F is the Faraday constant (96,485 C mol^{-1}); C_{total} is the corresponding total charge in coulombs in one test. In the MEA test, the liquid products from the cathode side were separated and collected by a cold trap. The FE for liquid products was calculated by collecting the products from both the anode and cathode sides during the same period.

The full-cell EE of C_2H_4 in the MEA was calculated by the following equation:

$$EE_{full\text{-}cell, C_2H_4} = \frac{\left(1.23 - E^\circ_{C_2H_4}\right) \times FE_{C_2H_4}}{E_{full\text{-}cell}}$$

where $E^\circ_{C_2H_4} = 0.17\,V$ is the equilibrium potential for CO to the C_2H_4 product[42]; and $E_{full\text{-}cell}$ is the full-cell voltage without ohmic loss correction in the MEA system.

The SPCE was calculated based on the following equation under 1 atm and 25 °C:

$$SPCE = \sum \frac{i\,(A) \times \frac{FE_C}{e_C} \times 0.01 \times 60\,(s)/F}{v_{CO\,inlet}\,(sccm)/24.5\,(l\,mol^{-1})/1,000}$$

where i is the total current; FE_C is the FE for a specific multicarbon product; v is the flow rate of inlet CO feed gas; and e is the number of electrons transferred per carbon atom in a specific multicarbon product (e_{C2H4}, $e_{ethanol}$, $e_{n\text{-propanol}} = 4$; $e_{acetate} = 2$).

Characterization
The morphologies of samples were recorded by scanning electron microscopy (Hitachi FE-SEM SU5000) and transmission electron microscopy (Hitachi H-7650). High-resolution transmission electron microscopy images and energy-dispersive X-ray spectroscopy elemental mapping were carried out on a Themis Z field-emission transmission electron microscope with an accelerating voltage of 200 kV. X-ray diffraction patterns were recorded with a MiniFlex600 with Cu Kα radiation ($\lambda = 1.54178$ Å). XPS measurements were carried out on PerkinElmer model 5600 with a monochromatic aluminium X-ray source. The binding energies were corrected for specimen charging by referencing C 1s to 284.6 eV. Electron paramagnetic resonance spectra were collected on a JES-FA200 (JEOL). Static contact angles were measured with Attension Theta tensiometers (Biolin Scientific). Diffuse reflectance infrared Fourier transform measurements were obtained using a Nicolet iS50 (Thermo Scientific).

Operando Raman measurements
Operando Raman measurements were conducted using a modified flow cell in 1 M LiOH electrolyte[43], which used a Renishaw inVia Raman microscope equipped with a water immersion objective (×63) lens with a 785 nm laser at 0.1% intensity. Each spectrum was recorded using the Renishaw WiRE (v.4.4) software by integrating twice, with each integration lasting 10 s. CO was continuously supplied to the gas chamber during the measurement. The potentials from the Raman measurements were converted to values versus RHE.

Operando X-ray absorption spectroscopy measurements
Operando X-ray absorption spectroscopy (XAS) measurements on the Cu-100TCNQ catalyst were carried out in fluorescence mode at the Australian Synchrotron (Clayton, Victoria, Australia), using a multipole wiggler XAS beamline (12-ID) with a home-made flow cell. The only difference compared to the flow cell used to evaluate the CORR performance is that we used Kapton tape to seal the gas chamber to admit X-ray irradiation and allow the fluorescent signal out. The XAS spectra were obtained for different galvanostatic conditions and were processed using ATHENA and ARTEMIE software included in the standard IFEFFIT package[44].

Computational methods
DFT was applied to investigate the ethylene production mechanism on copper and on TCNQ-modified copper surfaces. All the DFT calculations were carried out in the Vienna Ab initio Simulation Package with a plane-wave pseudopotential implementation[45,46].

The exchange-correlation functional was described by the spin-polarized generalized gradient approximation of Perdew–Burker–Ernzerhof and the electron–ion interactions were described by projector-augmented wave potentials[47,48]. A kinetic cut-off energy of 450 eV was used for the plane-wave expansion. $3 \times 2 \times 1$ and $6 \times 4 \times 1$ Monkhorst–Pack k-point meshes were used for geometry optimization and electronic structure calculation[49]. The long-range van de Waals interactions were described by the zero-damping DFT-D3 method of Grimme et al[50]. The Cu(111) surface was specifically selected because the (111) surface was found to be the dominant surface in the copper-based electrocatalyst material utilized in this work, which was confirmed by the X-ray diffraction measurements. A $6 \times 4 \times 4$ periodic cell of face-centred cubic Cu(111)-TCNQ surface was initially constructed for the TCNQ-modified copper surface. The Cu(111)-TCNQ surface with the lowest energy was used for the further investigation of the reactions. To decouple the interaction between them, a 15 Å vacuum space was created among the periodic surfaces in the z direction. To reduce the computational cost, only the metal atoms in the two uppermost layers and adsorbates were allowed to relax during the structural optimization calculations, whereas the atoms in the two bottom-most layers were fixed.

A computational hydrogen electrode model was used to calculate the Gibbs free energy by correcting the electronic energies directly determined from the DFT calculations with zero-point energies, entropies and heat capacities, which are calculated from the harmonic oscillator approximation at 298.15 K (ref. 51). The climbing-image nudged elastic band method was applied to search the transition state of H_2O dissociation on Cu(111) and Cu(111)-TCNQ surfaces, which were then verified by calculating the imaginary frequency[52]. A constant electrode potential model was utilized to consider the applied potential effects on the reaction mechanisms (Supplementary Fig. 40 and Supplementary Note 4).

The variation in charge-density was used to investigate the charge transfer between the *CHCOH intermediate and surface[53,54]. To study the effect of the TCNQ molecule on the interfacial water layer, 12 water molecules were introduced to Cu(111)-TCNQ surfaces. To optimize the interfacial water structure, ab initio molecular dynamics simulations were conducted in a canonical ensemble (NVT) for 15 ps with the Nosé–Hoover thermostat and a 1.0 fs time step at 300 K (refs. 55,56). DFT calculations were again performed to optimize the geometry from ab initio molecular dynamics to obtain the final interfacial water layer structure.

Multiphysics simulation methods
A modified Poisson–Boltzmann method, implemented in COMSOL (COMSOL Multiphysics v.6.2), was applied to calculate the distribution of the cations at the electrode–electrolyte interface. See Supplementary Note 3 for more details.

Data availability
All necessary data supporting the findings of this study are available in the Article and its Supplementary Information.

References

1. Yang, B. et al. Accelerating CO_2 electroreduction to multicarbon products via synergistic electric-thermal field on copper nanoneedles. *J. Am. Chem. Soc.* **144**, 3039–3049 (2022).
2. Liu, W. et al. Electrochemical CO_2 reduction to ethylene by ultrathin CuO nanoplate arrays. *Nat. Commun.* **13**, 1877 (2022).
3. Xia, R., Overa, S. & Jiao, F. Emerging electrochemical processes to decarbonize the chemical industry. *JACS Au* **2**, 1054–1070 (2022).
4. Chen, X. et al. Electrochemical CO_2-to-ethylene conversion on polyamine-incorporated Cu electrodes. *Nat. Catal.* **4**, 20–27 (2020).
5. Li, P. et al. *p–d* orbital hybridization induced by *p*-block metal-doped Cu promotes the formation of C_{2+} products in ampere-level CO_2 electroreduction. *J. Am. Chem. Soc.* **145**, 4675–4682 (2023).
6. Gu, J. et al. Modulating electric field distribution by alkali cations for CO_2 electroreduction in strongly acidic medium. *Nat. Catal.* **5**, 268–276 (2022).
7. Zhao, Y. et al. Conversion of CO_2 to multicarbon products in strong acid by controlling the catalyst microenvironment. *Nat. Synth.* **2**, 403–412 (2023).
8. She, X. et al. Pure-water-fed, electrocatalytic CO_2 reduction to ethylene beyond 1,000 h stability at 10 A. *Nat. Energy* **9**, 81–91 (2024).
9. Rabinowitz, J. A. & Kanan, M. W. The future of low-temperature carbon dioxide electrolysis depends on solving one basic problem. *Nat. Commun.* **11**, 5231 (2020).
10. Jouny, M., Hutchings, G. S. & Jiao, F. Carbon monoxide electroreduction as an emerging platform for carbon utilization. *Nat. Catal.* **2**, 1062–1070 (2019).
11. Zhu, P. et al. Direct and continuous generation of pure acetic acid solutions via electrocatalytic carbon monoxide reduction. *Proc. Natl Acad. Sci. USA* **118**, e2010868118 (2021).
12. Ozden, A. et al. Cascade CO_2 electroreduction enables efficient carbonate-free production of ethylene. *Joule* **5**, 706–719 (2021).
13. Wei, P. et al. Coverage-driven selectivity switch from ethylene to acetate in high-rate CO_2/CO electrolysis. *Nat. Nanotechnol.* **18**, 299–306 (2023).
14. Zhang, J. et al. Steering CO_2 electroreduction pathway toward ethanol via surface-bounded hydroxyl species-induced noncovalent interaction. *Proc. Natl Acad. Sci. USA* **120**, e2218987120 (2023).
15. Zhu, H.-L. et al. A porous π–π stacking framework with dicopper(I) sites and adjacent proton relays for electroreduction of CO_2 to C_{2+} products. *J. Am. Chem. Soc.* **144**, 13319–13326 (2022).
16. Goyal, A. & Koper, M. T. M. The interrelated effect of cations and electrolyte pH on the hydrogen evolution reaction on gold electrodes in alkaline media. *Angew. Chem. Int. Ed.* **60**, 13452–13462 (2021).
17. Li, P. et al. Hydrogen bond network connectivity in the electric double layer dominates the kinetic pH effect in hydrogen electrocatalysis on Pt. *Nat. Catal.* **5**, 900–911 (2022).
18. Liu, E. et al. Unifying the hydrogen evolution and oxidation reactions kinetics in base by identifying the catalytic roles of hydroxyl-water-cation adducts. *J. Am. Chem. Soc.* **141**, 3232–3239 (2019).
19. Kumar, S., Hoshino, M., Kerkeni, B., García, G. & Limão-Vieira, P. Isotope effect in D_2O negative ion formation in electron transfer experiments: DO–D bond dissociation energy. *J. Phys. Chem. Lett.* **14**, 5362–5369 (2023).
20. Andersson, K., Nikitin, A., Pettersson, L. G. M., Nilsson, A. & Ogasawara, H. Water dissociation on Ru(001): an activated process. *Phys. Rev. Lett.* **93**, 196101 (2004).
21. Li, J. et al. Electrokinetic and in situ spectroscopic investigations of CO electrochemical reduction on copper. *Nat. Commun.* **12**, 3264 (2021).
22. Liang, Y. et al. Stabilizing copper sites in coordination polymers toward efficient electrochemical C–C coupling. *Nat. Commun.* **14**, 474 (2023).
23. Shao, F. et al. Surface water as an initial proton source for the electrochemical CO reduction reaction on copper surfaces. *Angew. Chem. Int. Ed.* **62**, e202214210 (2023).
24. Li, Y. et al. Interstitial boron-triggered electron-deficient Os aerogels for enhanced pH-universal hydrogen evolution. *Nat. Commun.* **13**, 1143 (2022).
25. Strmcnik, D. et al. Improving the hydrogen oxidation reaction rate by promotion of hydroxyl adsorption. *Nat. Chem.* **5**, 300–306 (2013).
26. Dong, Y. et al. Efficient water dissociation on confined ultrafine Pt via pyridinic N-enhanced heavy *d–π* interaction. *Chem. Mater.* **34**, 8271–8279 (2022).
27. Xie, Y. et al. Boosting water dissociation kinetics on Pt–Ni nanowires by N-induced orbital tuning. *Adv. Mater.* **31**, 1807780 (2019).
28. Blowey, P. J. et al. Alkali doping leads to charge-transfer salt formation in a two-dimensional metal–organic framework. *ACS Nano* **14**, 7475–7483 (2020).
29. Otero, R., Miranda, R. & Gallego, J. M. A comparative computational study of the adsorption of TCNQ and F_4-TCNQ on the coinage metal surfaces. *ACS Omega* **4**, 16906–16915 (2019).
30. Tseng, T.-C. et al. Charge-transfer-induced structural rearrangements at both sides of organic/metal interfaces. *Nat. Chem.* **2**, 374–379 (2010).
31. Mahajan, M., Bhargava, S. K. & O'Mullane, A. P. Reusable surface confined semi-conducting metal-TCNQ and metal-$TCNQF_4$ catalysts for electron transfer reactions. *RSC Adv.* **3**, 4440–4446 (2013).
32. Wang, N. et al. Boride-derived oxygen-evolution catalysts. *Nat. Commun.* **12**, 6089 (2021).
33. Overa, S. et al. Enhancing acetate selectivity by coupling anodic oxidation to carbon monoxide electroreduction. *Nat. Catal.* **5**, 738–745 (2022).
34. Ding, P. et al. Elucidating the roles of Nafion/solvent formulations in copper-catalyzed CO_2 electrolysis. *ACS Catal.* **13**, 5336–5347 (2023).
35. Gunathunge, C. M., Li, J., Li, X. & Waegele, M. M. Surface-adsorbed CO as an infrared probe of electrocatalytic interfaces. *ACS Catal.* **10**, 11700–11711 (2020).
36. Zhang, T., Yuan, B., Wang, W., He, J. & Xiang, X. Tailoring *H intermediate coverage on the $CuAl_2O_4$/CuO catalyst for enhanced electrocatalytic CO_2 reduction to ethanol. *Angew. Chem. Int. Ed.* **135**, e202302096 (2023).
37. An, H. et al. Sub-second time-resolved surface-enhanced Raman spectroscopy reveals dynamic CO intermediates during electrochemical CO_2 reduction on copper. *Angew. Chem. Int. Ed.* **60**, 16576–16584 (2021).
38. Patra, K. K. et al. Operando spectroscopic investigation of a boron-doped CuO catalyst and its role in selective electrochemical C–C coupling. *ACS Appl. Energy Mater.* **3**, 11343–11349 (2020).
39. Xiao, H., Cheng, T. & Goddard, W. A. Atomistic mechanisms underlying selectivities in C_1 and C_2 products from electrochemical reduction of CO on Cu(111). *J. Am. Chem. Soc.* **139**, 130–136 (2017).
40. Li, F. et al. Cooperative CO_2-to-ethanol conversion via enriched intermediates at molecule-metal catalyst interfaces. *Nat. Catal.* **3**, 75–82 (2020).
41. Li, Z. et al. Room-temperature high-performance H_2S sensor based on porous CuO nanosheets prepared by hydrothermal method. *ACS Appl. Mater. Interfaces* **8**, 20962–20968 (2016).

42. Wang, X. et al. Efficient electrosynthesis of *n*-propanol from carbon monoxide using a Ag–Ru–Cu catalyst. *Nat. Energy* **7**, 170–176 (2022).

43. Li, F. et al. Molecular tuning of CO_2-to-ethylene conversion. *Nature* **577**, 509–513 (2020).

44. Ravel, B. & Newville, M. ATHENA, ARTEMIS, HEPHAESTUS: data analysis for X-ray absorption spectroscopy using IFEFFIT. *J. Synchrotron Rad.* **12**, 537–541 (2005).

45. Kresse, G. & Furthmüller, J. Efficient iterative schemes for ab initio total-energy calculations using a plane-wave basis set. *Phys. Rev. B* **54**, 11169–11186 (1996).

46. Payne, M. C., Teter, M. P., Allan, D. C., Arias, T. A. & Joannopoulos, J. D. Iterative minimization techniques for ab initio total-energy calculations: molecular dynamics and conjugate gradients. *Rev. Mod. Phys.* **64**, 1045–1097 (1992).

47. Blöchl, P. E. Projector augmented-wave method. *Phys. Rev. B* **50**, 17953–17979 (1994).

48. Kresse, G. & Joubert, D. From ultrasoft pseudopotentials to the projector augmented-wave method. *Phys. Rev. B* **59**, 1758–1775 (1999).

49. Monkhorst, H. J. & Pack, J. D. Special points for Brillouin-zone integrations. *Phys. Rev. B* **13**, 5188–5192 (1976).

50. Grimme, S., Antony, J., Ehrlich, S. & Krieg, H. A consistent and accurate ab initio parametrization of density functional dispersion correction (DFT-D) for the 94 elements H–Pu. *J. Chem. Phys.* **132**, 154104 (2010).

51. Nørskov, J. K. et al. Origin of the overpotential for oxygen reduction at a fuel-cell cathode. *J. Phys. Chem. B* **108**, 17886–17892 (2004).

52. Henkelman, G., Uberuaga, B. P. & Jónsson, H. A climbing image nudged elastic band method for finding saddle points and minimum energy paths. *J. Chem. Phys.* **113**, 9901–9904 (2000).

53. Bader, R. F. W. A quantum theory of molecular structure and its applications. *Chem. Rev.* **91**, 893–928 (1991).

54. Tang, W., Sanville, E. & Henkelman, G. A grid-based Bader analysis algorithm without lattice bias. *J. Phys. Condens. Matter* **21**, 084204 (2009).

55. Hoover, W. G. Canonical dynamics: equilibrium phase-space distributions. *Phys. Rev. A* **31**, 1695–1697 (1985).

56. Nosé, S. Constant temperature molecular dynamics methods. *Prog. Theor. Phys. Supp.* **103**, 1–46 (1991).

Author contributions

E.H.S, D.S., J.Z. and Fengwang Li supervised the project. Y. Liang synthesized the catalysts and performed all the electrochemical experiments. Feng Li carried out the DFT calculations, ab initio molecular dynamics simulation, and multiphysics simulation. P.O. and X.-Y.L. participated in the computational data analysis. R.K.M performed the cascade system modelling and calculated the energy cost. S.H. performed transmission electron microscopy, high-resolution transmission electron microscopy and energy-dispersive X-ray spectroscopy mapping experiments. W.N. and S.P. assisted in electrochemical and operando Raman experiments. S.Z. conducted the operando XAS experiments. Y. Liu carried out the XPS experiments. Y.B. contributed to the CORR isotope experiments and data analysis. H.W. assisted in the X-ray diffraction experiments. N.W. provided the NiFe-B anode catalysts. Y. Liang, E.H.S., Fengwang Li and D.S. co-wrote and edited the manuscript. All authors discussed the results and assisted during the manuscript preparation.

Competing interests

The authors declare no competing interests.

Additional information

Supplementary information The online version contains supplementary material available at https://doi.org/10.1038/s44160-024-00568-8.

Correspondence and requests for materials should be addressed to Fengwang Li, Jie Zeng, David Sinton or Edward H. Sargent.

Peer review information *Nature Synthesis* thanks Yongji Gong and the other, anonymous, reviewer(s) for their contribution to the peer review of this work. Primary Handling Editor: Alexandra Groves, in collaboration with the *Nature Synthesis* team.

Reprints and permissions information is available at www.nature.com/reprints.

Publisher's note Springer Nature remains neutral with regard to jurisdictional claims in published maps and institutional affiliations.